LANGMUIR

pubs.acs.org/Langmuir Article

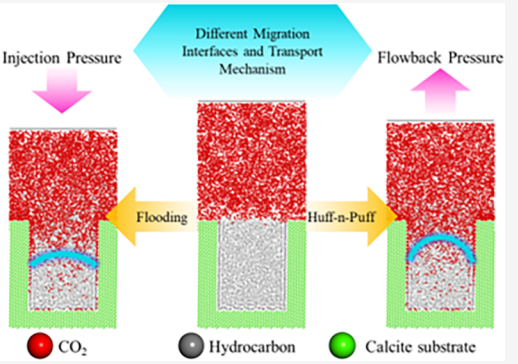
Molecular Insights into CO_2 Flooding and Huff-and-Puff for Enhanced Shale Oil Recovery and Carbon Sequestration in Dead-End Nanopores

Shiqiang Guo, Keliu Wu,* Qingyuan Zhu, Dong Feng, Juan Luo, Shengting Zhang, Linghao Peng, Yaowei Huang, Ke Xu, and Zhehui Jin*

Cite This: *Langmuir* 2026, 42, 4029–4042 Read Online

ACCESS | Metrics & More | Article Recommendations | Supporting Information

ABSTRACT: CO_2 injection for enhanced oil recovery (EOR) and geological carbon sequestration (GCS) in shale reservoirs offers a promising win-win strategy. Yet, the mechanisms by which CO_2 flooding and huff-and-puff (HNP) mobilize multicomponent shale oil in inorganic nanopores remain unclear, particularly regarding their respective contributions to oil recovery and CO_2 storage. Here, we employ molecular dynamics (MD) simulations to compare CO_2 flooding and HNP in calcite dead-end nanopores saturated with a multicomponent hydrocarbon mixture. We analyze interfacial and transport behaviors, extract localized molecular clusters to quantify self-diffusion coefficients, and examine the roles of flood and flowback pressures. Results show that flooding promotes greater CO_2 penetration into nanopores but suppresses counter-current hydrocarbon migration, limiting swelling-driven recovery. In contrast, HNP enables CO_2 diffusion during the huff stage and reverse pressure gradients during the puff stage, which enhance oil swelling and achieve higher recovery at the expense of lower storage efficiency. Elevated CO_2 density increases the diffusion coefficients of all components, underscoring the critical roles of pressure gradients and molecular transport. By extracting localized molecular clusters, we further obtained pressure-dependent diffusion bounds for CO_2 and hydrocarbons and quantify injection and flowback pressure windows that jointly optimize oil recovery and the CO_2 storage efficiency. On this basis, we propose a well-count-agnostic and field translatable hybrid method that achieves 60.44% oil recovery and 47.18% CO_2 storage efficiency. These findings provide molecular-scale guidance for full-process CCUS design in unconventional reservoirs.



1. INTRODUCTION

The rapid pace of industrial development and the rising global energy demand have led to a sharp increase in greenhouse gas emissions, particularly CO_2, accelerating climate change and posing serious risks to ecosystems and human societies.[1−3] As a result, reducing CO_2 emissions has become a global priority.[4−6] Among various mitigation strategies, carbon capture, utilization, and storage (CCUS) has gained increasing attention, especially in the petroleum sector, as a promising route toward carbon neutrality.[7] Notably, CCUS can both enhance oil recovery (EOR) and provide long-term geological storage for CO_2,[8−10] potentially contributing over 15% of global CO_2 emission reductions.[11]

On the other hand, the shale-driven unconventional oil and gas revolution has greatly advanced energy security.[12−14] Shale reservoirs, unlike conventional ones, are dominated by nanopores with extremely small pore sizes, complex geometries, and ultralow permeability.[15,16] These features result in strong confinement effects,[17,18] that influence fluid distribution and flow behavior,[19] making efficient development challenging.[20] A significant portion of shale oil is retained in adsorbed states within these nanopores.[21] Recent studies have demonstrated that CO_2 injection can mobilize this adsorbed oil by promoting desorption into the free phase, enhancing oil recovery.[22,23] At the same time, the extensive nanoporous network provides substantial capacity for CO_2 sequestration.[24] Therefore, CO_2-EOR in shale reservoirs presents a promising dual solution for both oil recovery and geological carbon storage (GCS), and it remains an active area of research.

CO_2 is an effective flooding agent due to its low viscosity, high density, and strong mobility.[25] It enhances oil recovery through mechanisms such as dissolution and diffusion,[26] oil swelling,[27] viscosity reduction,[28] desorption,[29] and miscibility.[30,31] Achieving both high oil recovery and high CO_2 storage

Received: October 21, 2025
Revised: January 14, 2026
Accepted: January 15, 2026
Published: January 21, 2026



ACS Publications © 2026 American Chemical Society

https://doi.org/10.1021/acs.langmuir.5c05534
Langmuir 2026, 42, 4029−4042

Downloaded from pubs.acs.org/langd5/article-pdf/42/5/4029/6424108/la5c05534.pdf by PEKING UNIV user on 11 November 2026

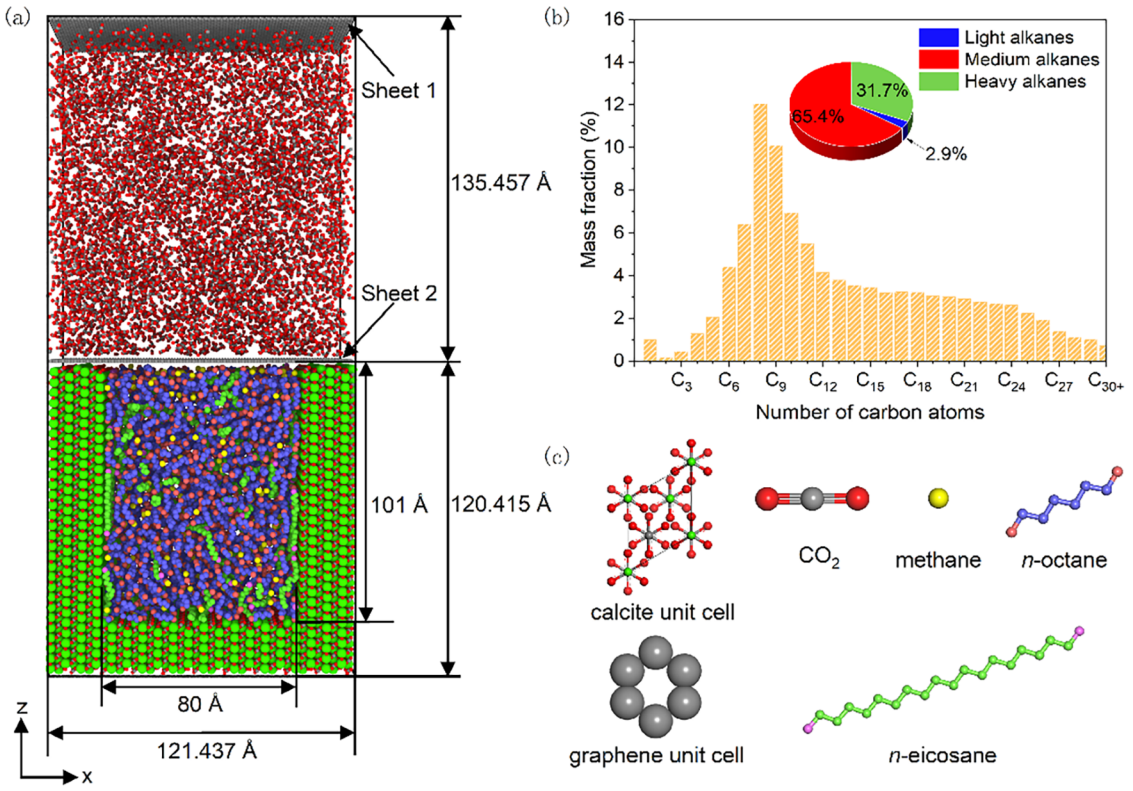


Figure 1. (a) Initial configuration of the model, (b) experimental results of shale oil components composition, and (c) molecular structures of calcite unit cell, CO_2, and hydrocarbons. Color scheme: green, calcium atoms in calcite; red, oxygen atoms; gray, carbon atoms; yellow, CH_4; light red and pink, $-CH_3$ group; blue and light green, $-CH_2$ group.

efficiency requires optimizing the injection strategies. Two main CO_2 injection approaches, continuous flooding and huff-and-puff (HNP), have shown promise in shale reservoirs.[32−35] Core flooding experiments have evaluated key parameters such as injection rate,[36] injection and flowback pressures,[37] soaking time,[38] and the number of HNP cycles.[39] Microfluidic studies have further revealed that CO_2 can effectively mobilize oil from small and medium pores.[40] Numerical simulations have examined the influence of CO_2 diffusion,[41] reservoir properties,[42] and fluid characteristics.[43] For instance, Wang et al.[44] used a multiple-relaxation-time lattice Boltzmann method (MRT-LBM) to simulate diffusion, adsorption, and miscible flow of CO_2-oil systems at the pore scale, with validation from molecular dynamics (MD) simulations. However, the accuracy of such models depends on reliable molecular-level insights.[45]

In this context, MD simulations have become a powerful tool for probing molecular-scale interactions that govern macroscopic behaviors.[46,47] For example, prior studies have shown that CO_2 preferentially adsorbs onto pore surfaces in competition with single-component hydrocarbon.[48−50] However, real shale oil is a complex multicomponent system. Additionally, many investigations focus on connected calcite nanopores, where CO_2 has demonstrated significant extraction efficiency.[29,51,52] Yet, shale formations also contain abundant dead-end calcite nanopores, which trap residual oil and are thus critical for further recovery enhancement.[53] Oil transport in these isolated pores is kinetically hindered, resulting in concentration gradients and limited mass transfer, key factors in the development strategy effectiveness. These pores also serve as potential "microreservoirs" for long-term CO_2 storage. Most recently, Chen et al.[54] designed an extended bulk pore, a nanochannel and a dead-end pore system to explain excessive water cut during cyclic gas injection, highlighting how heavy-component condensation in the pore throat traps water and controls HNP performance. Wang et al.[55] simulated CO_2 HNP of multicomponent hydrocarbons in a calcite dead-end nanopore. They found that CO_2 enters primarily via diffusion, preferentially adsorbs onto the surface, displaces methane and *n*-octane, but fails to effectively strip asphaltenes. The study also highlighted the importance of pressure gradients and diffusion as key drivers for oil recovery, with higher injection pressures, lower flowback pressures, and larger pore sizes improving performance. While insightful, these studies did not compare the mechanistic differences between flooding and HNP, nor did they provide detailed analysis of transport behaviors and compositional evolution of individual oil components, both of which are crucial for method selection and optimization.

In this work, we employ MD simulations to systematically compare CO_2 flooding and HNP for a simplified shale oil mixture (CH_4, nC_8, and nC_{20}) confined in calcite dead-end nanopores. We analyze both flooding and HNP methods under consistent conditions and capture the interfacial evolution and transport behavior of each hydrocarbon component. By extracting local molecular clusters from nonequilibrium simulations, we quantify pressure-dependent self-diffusion bounds for CO_2 and hydrocarbons and determine injection and flowback pressure windows that jointly optimize oil recovery and CO_2 storage efficiency. Based on these insights, we propose a well-count-agnostic hybrid method that maximizes oil recovery while maintaining high CO_2 storage efficiency and is readily translatable to field operations. These insights not only support the design of optimized shale development schemes but also provide molecular-level

https://doi.org/10.1021/acs.langmuir.5c05534
Langmuir 2026, 42, 4029−4042

Downloaded from pubs.acs.org/langd5/article-pdf/42/5/4029/6424108/la5c05534.pdf by PEKING UNIV user on 11 November 2026

Table 1. Simulation Details, Including Development Approach, Injection Pressure, Flowback Pressure, External Forces, and Simulation Duration

case	approach	injection pressure, MPa	external forces, kcal/mol·Å	simulation duration, ns	flowback pressure, MPa	external forces, kcal/mol·Å	simulation duration, ns
1	CO_2 flooding	26 MPa	0.00972	12	/	/	/
2	CO_2 flooding	29 MPa	0.01085	12	/	/	/
3	CO_2 HNP	23 MPa	0.00857	6	20 MPa	0.00745	6
4	CO_2 HNP	23 MPa	0.00857	6	17 MPa	0.00633	6

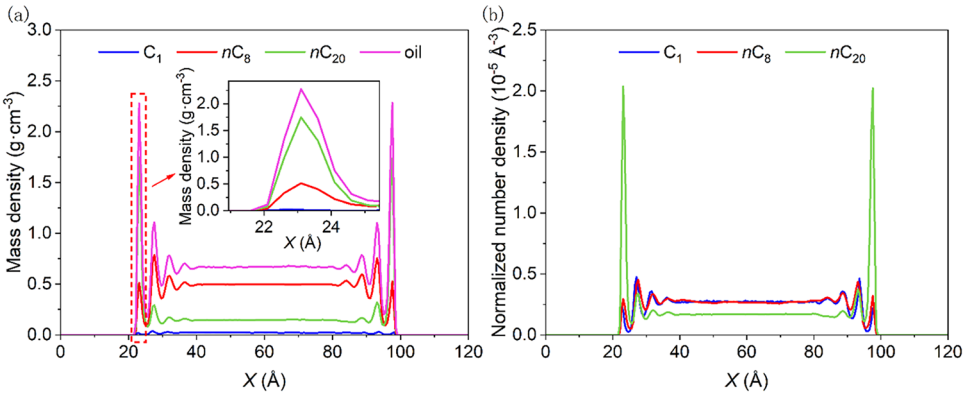


Figure 2. (a) Mass density and (b) normalized molecular number density distribution of each hydrocarbon component. The oil refers to a combination of methane, *n*-octane, and *n*-eicosane ($\rho_oil = \rho_C_1 + \rho_nC_8 + \rho_nC_{20}$).

inputs and validation for larger-scale modeling frameworks such as LBM simulations.

2. EXPERIMENTAL SECTION

2.1. Molecular Models

In this study, we constructed an MD model to investigate oil displacement by supercritical CO_2 (Sc-CO_2) in a dead-end nanopore, as shown in Figure 1a. Calcite was chosen as the solid substrate, which is a typical mineral in the target shale oil reservoir.[56] Its crystal structure belongs to the carbonate mineral of the trigonal crystal system, with the chemical formula $CaCO_3$. The unit cell exhibits a rhombohedral structure, with parameters $a = b = 4.990$ Å and $c = 17.061$ Å, and angles $\alpha = \beta = 90°$ and $\gamma = 120°$. The crystal was cut along the $(10\ \bar{4})$ plane to obtain a stable crystal surface.[57,58] The unit cell was then replicated to $x = 121.437$ Å, $y = 49.900$ Å, and $z = 120.415$ Å. A dead-end nanopore substrate model was generated by moving part of the calcite atoms with width, $w = 80$ Å and depth, $h = 101$ Å. Then, crude oil was introduced into a dead-end nanopore. We experimentally obtained the crude oil composition of the target shale reservoir, as shown in Figure 1b. Accordingly, methane (C_1), *n*-octane (nC_8), and *n*-eicosane (nC_{20}) were selected to represent the light (C_1–C_4), medium (C_5–C_{16}), and heavy (C_{17}–C_{30+}) hydrocarbons (Figure 1c), respectively. The external environment of the nanopore represents larger pores or fractures, where a large number of injected CO_2 molecules were placed. A single graphene six-membered-ring array was replicated and placed above the CO_2 molecule (Sheet 1) and a dead-end nanopore (Sheet 2). Initially, an external force was applied to Sheets 1 and 2 along the negative *Z* direction to regulate system pressure. When the system reached equilibrium, Sheet 2 was then removed, and varying external forces were applied to Sheet 1 to simulate the CO_2 injection process. We note that the graphene sheets exert only repulsive forces throughout the process.

2.2. Force Field Parameters

Calcite is modeled using the force field parameters developed by Xiao et al.[59], which have been demonstrated to be highly suitable for calcite-hydrocarbon systems and accurately capture fluid–solid interactions.[55,60] Hydrocarbon molecules are described using the Optimized Potential for Liquid Simulations-United Atom (OPLS-UA) force field,[61] which is widely applied in organic molecular systems. CO_2 is modeled using the Transferable Potentials for Phase Equilibria (TraPPE) force field,[62] where the molecule is treated as rigid, with no intramolecular interactions. Detailed force field parameters are provided in Tables S1 and S2 in Supporting Information (SI).

2.3. Simulation Details

Energy minimization of the constructed MD model was first performed using the conjugate gradient algorithm to eliminate any unfavorable molecular configurations, with energy and force tolerances of 1.0×10^{-6} and 1.0×10^{-8}, respectively. A Nosé-Hoover thermostat maintained the system temperature at 363.95 K.[63] The system pressure is controlled by applying varying forces to graphene sheets along the *Z* axis. To match the target reservoir conditions, the equilibrium pore pressure was set to 23 MPa. Flooding was conducted at 26 and 29 MPa. For HNP, the huff stage was maintained at 23 MPa, followed by the puff stage at 20 and 17 MPa. Overall, a 10 ns equilibrium molecular dynamics (EMD) simulation followed to achieve a stable configuration. Subsequently, external-force-driven nonequilibrium molecular dynamics (EF-NEMD) simulations were conducted to model CO_2 flooding and HNP processes with the total simulation time of 12 ns.[64−66] The calcite substrate was held fixed throughout the simulation. Simulation details are listed in Table 1.

In this study, all MD simulations were conducted using the open source software Large-scale Atomic/Molecular Massively Parallel Simulation (LAMMPS).[67] Initial fluid-molecule configurations were generated with the Moltemplate toolkit,[68] and trajectory visualization and rendering were performed in the open Visualization Tool (OVITO).[69] Simulations were performed in the *NVT* ensemble. The interactions between different atoms were calculated using the Lorentz–Berthelot mixing criterion, and the long-range Coulombic interactions were computed by the particle–particle and particle-mesh (PPPM) algorithm with an accuracy of 1.0 × 10−4.[70] Periodic boundary conditions were imposed in the *X* and *Y* directions. All intermolecular interactions were cut off at 12 Å, and the time step was set to 1.0 fs. To minimize spurious electrostatic interactions during the simulation, a vacuum layer exceeding 200 Å was added along the *Z* direction.

Downloaded from pubs.acs.org/langd5/article-pdf/42/5/4029/6424108/la5c05534.pdf by PEKING UNIV user on 11 November 2026

https://doi.org/10.1021/acs.langmuir.5c05534
Langmuir 2026, 42, 4029−4042

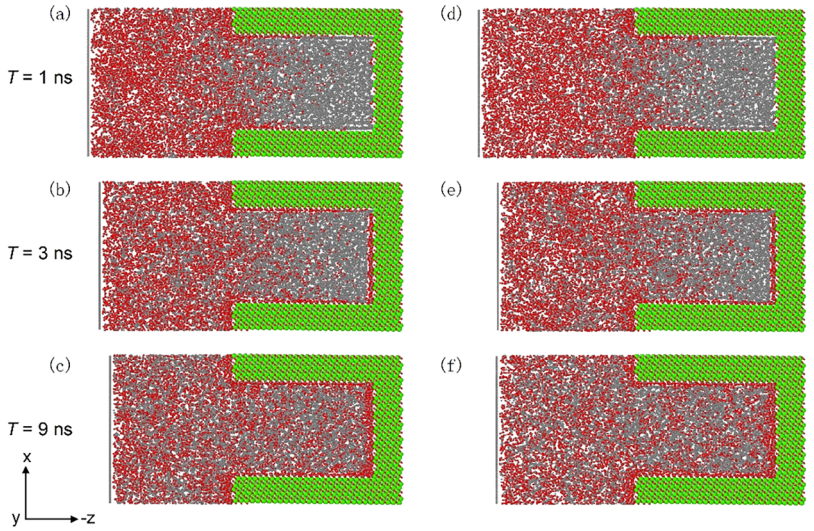


Figure 3. Simulation snapshots on $X-Z$ plane of (a–c) CO_2 flooding and (d–f) CO_2 HNP in shale calcite dead-end nanopore at 1, 3, and 9 ns, respectively. For display convenience, these models are rotated by 90°. To enhance visual clarity of CO_2 and hydrocarbons transport, we employ a simplified coloring scheme: gray, carbon atoms and all hydrocarbons; red, oxygen atoms.

3. RESULTS AND DISCUSSION

In this section, we first analyze the simulation results of CO_2 flooding and HNP processes within a calcite dead-end nanopore. We then compare the interfacial and transport behaviors of multicomponent hydrocarbons and CO_2 between two injection approaches and systematically elucidate the mechanisms governing oil displacement and enhanced mobility, including molecular diffusion, competitive adsorption, dissolution, and oil swelling. Finally, we examine the effects of injection pressure and flowback pressure on oil recovery and CO_2 storage efficiency, helping identify optimized schemes and propose synergistic approaches for different production stages to further enhance both recovery and storage.

3.1. Occurrence State of Shale Oil

After a 10 ns relaxation, we calculate the mass density and the normalized molecular number density distributions of multicomponent hydrocarbons along the X direction in a calcite dead-end nanopore prior to CO_2 injection using (eqs 1 and 2). Normalization eliminates the molecular number bias and thus better captures the relative adsorption strengths at the calcite surface.[55] The results are listed in Figure 2. It is evident that hydrocarbon density near the substrate exceeds that in the pore center. C_1, nC_8, and nC_{20} each form multiple adsorption layers, indicating a strong affinity between hydrocarbons and the calcite substrate. The adsorption capacities of each hydrocarbon component are shown in Figure 2b. nC_{20} exhibits the highest adsorption peak ($\approx 2.04 \times 10^{-5}$ Å^{-3}), confirming that heavy hydrocarbons adhere most strongly to the substrate. In contrast, the adsorption peak of C_1 and nC_8 is much lower ($\approx 0.5 \times 10^{-5}$ Å^{-3}), suggesting that a small number of them occupy the interstices between nC_{20} layers and the substrate, with the majority remaining in the pore center.

$$\rho(\vec{x})_{\text{Mass}} = \frac{\overline{m_i} \times 10^{21}}{\triangle x \times Ly \times Lz} \tag{1}$$

$$\rho(\vec{x})_{\text{Number-nor}} = \frac{\overline{N_i} \times 10^{21}}{\triangle x \times Ly \times Lz \times M_i \times N_{i-\text{total}}} \tag{2}$$

where ρ_{Mass} represents the mass density, g·cm^{-3} and $\rho_{\text{Number-nor}}$ represents the normalized molecular number density, cm^{-3}. $\overline{m_i}$ represents the average molecular mass of the i-th component within each bin, g. Δx represents the bin size along the X direction, 0.5 Å. L_y and L_z are the lengths of the graphene sheet in the Y direction and Z direction, respectively, Å. $\overline{N_i}$ represents the average number of atoms of the i-th component within each bin. M_i represents the number of atoms in a single molecule of the i-th component. $N_{i\text{-total}}$ represents the total number of molecules of the i-th component.

We observe competitive adsorption among hydrocarbons, with the heavy hydrocarbon preferentially adsorbing on the calcite surface due to its strongest van der Waals interactions, while light and medium hydrocarbons are confined to occupying the remaining interstices. These findings corroborate previous observations that a substantial fraction of shale oil resides in an adsorbed state, in which heavy components preferentially form layered structures on the substrate, while light and medium components can adsorb within the interstices of these layered structures but predominantly reside in the bulk.[71,72]

3.2. Displacement Process during CO_2 Flooding and HNP

Figure 3 presents simulation snapshots at different times during the CO_2 flooding and HNP. Once Sheet 2 is removed, CO_2 rapidly dissolves into the hydrocarbons and penetrates the nanopore. The corresponding 2D density contours of oil (Figure 4) and CO_2 (Figure S6) show that, in the early stages of both flooding and HNP, a distinct hydrocarbon adsorption layer forms on the substrate. As CO_2 molecules enter the pore, they progressively displace hydrocarbons from the adsorption sites and establish a stable CO_2 adsorption layer. This displacement is driven by steric hindrance among hydrocarbon molecules combined with the strong affinity of calcite for CO_2. As a result, the adsorbed hydrocarbon layer gradually decreases in density, while CO_2 near the substrate exhibits a higher migration velocity compared with that in the pore center.[49,51,60] This behavior confirms competitive adsorption between CO_2 and hydrocarbons, where preferential CO_2 adsorption accelerates hydrocarbon desorption. By approximately 5.0 ns, the CO_2 has completely displaced the first

https://doi.org/10.1021/acs.langmuir.5c05534
Langmuir 2026, 42, 4029–4042

Downloaded from pubs.acs.org/langd5/article-pdf/42/5/4029/6424108/la5c05534.pdf by PEKING UNIV user on 11 November 2026

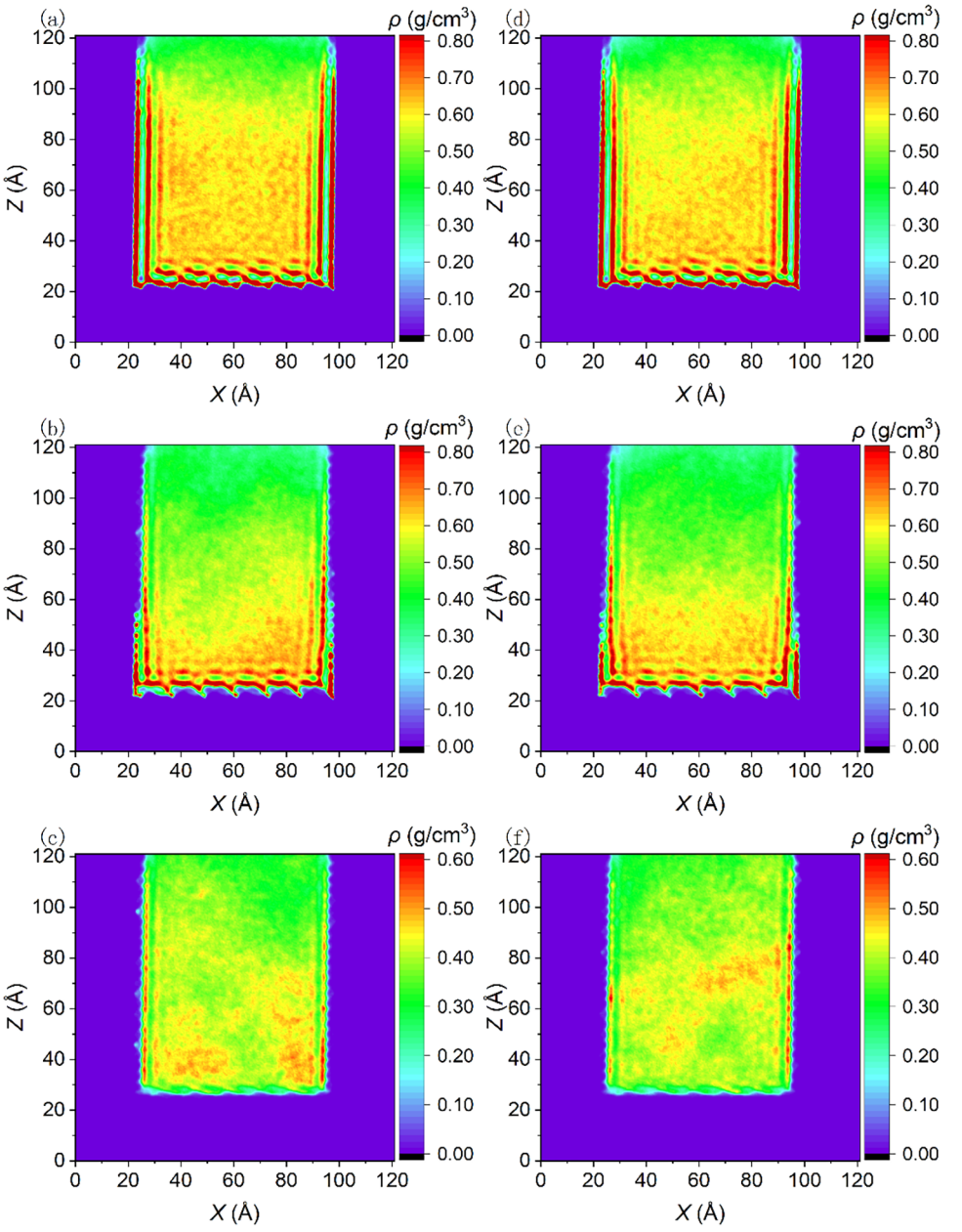


Figure 4. 2-D oil density contours on $X-Z$ plane of (a–c) CO_2 flooding and (d–f) CO_2 HNP in shale calcite dead-end nanopore at 1, 3, and 9 ns, respectively.

adsorbed hydrocarbon layer. The temporal evolution of each component during flooding and HNP is shown in Figure S7. Both the number of CO_2 molecules inside the dead-end nanopore and the number of hydrocarbons outside the pore increase over time. However, HNP mobilizes more hydrocarbons than flooding. This difference arises because the pressure gradient during flooding not only impedes hydrocarbon migration but also forces additional CO_2 molecules into the pore.

3.3. Interfacial and Transport Behavior of CO_2 and Hydrocarbon

To elucidate the oil displacement mechanisms of CO_2 flooding and HNP in calcite nanopore, we systematically compare the potential energy, radial density distributions, velocities, and diffusion coefficients of multicomponent hydrocarbons and CO_2 under both approaches. Then, the relative effectiveness of flooding versus HNP is quantified through analyzing the variation of oil recovery and CO_2 storage efficiency.

CO_2 injection into shale nanopores enhances oil recovery through favorable CO_2-oil interactions, but under confinement, interfacial and transport behaviors become highly complex. To probe the underlying mechanisms, we calculated the potential energy of CO_2 and oil, where a lower potential energy corresponds to greater stability. Figure 5 compares the potential energy of CO_2 and oil during flooding and HNP. As simulation time increases, the CO_2 potential energy decreases while the oil potential energy increases. This trend reflects CO_2 dissolution into the oil phase, which reduces the effective molecular free path, while hydrocarbons disentangle, desorb, and migrate outward, thereby increasing intermolecular distances and activity space. The net effect is oil swelling

Downloaded from pubs.acs.org/langd5/article-pdf/42/5/4029/6424108/la5c05534.pdf by PEKING UNIV user on 11 November 2026

https://doi.org/10.1021/acs.langmuir.5c05534
Langmuir 2026, 42, 4029–4042

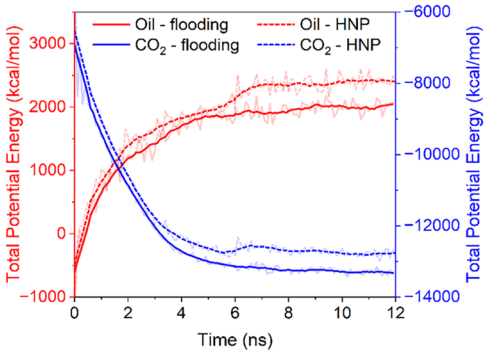


Figure 5. Total potential energy of CO_2 and oil of CO_2 flooding and CO_2 HNP.

and viscosity reduction, which macroscopically manifests as enhanced recovery.[73]

Comparing the two injection approaches revealed notable differences. During flooding, both CO_2 and hydrocarbons exhibit lower potential energy, and the increase in hydrocarbon potential energy is more gradual. This occurs because the forward pressure gradient (external pressure exceeding pore pressure) drives more CO_2 molecules into the pore, displacing adsorbed hydrocarbons and shortening the CO_2 free path. At the same time, this pressure gradient suppresses the migration of hydrocarbon out of the pore. By contrast, during HNP, the huff stage is dominated by CO_2 diffusion, leading to fewer CO_2 molecules inside the pore relative to flooding. Consequently, the CO_2 potential energy remains slightly higher, while hydrocarbons experience less resistance to outward migration, resulting in higher hydrocarbon potential energy. In the subsequent puff stage, the reverse pressure gradient promotes hydrocarbon outflow, reflected in a further rise in hydrocarbon potential energy. During this stage, partial CO_2 backflow causes transient fluctuations in the CO_2 potential energy before it stabilizes at a lower level. Overall, these potential energy trends suggest that oil mobilization is somewhat more difficult during flooding than during HNP. However, the deeper CO_2 penetration achieved in flooding may enhance the long-term storage capacity.

Oil swelling primarily manifests as hydrocarbon chain disentanglement and looser molecular distribution. To quantify this behavior, we calculated the radial density distribution (RDD), an analogue of the radial distribution function (RDF), which reflects clustering characteristics between CO_2 and hydrocarbons.[49] Figure 6a shows the RDDs between carbon atoms of different hydrocarbons, while Figure 6b shows the RDDs between CO_2 and hydrocarbons. In Figure 6a, both the peak height and integrated intensity of the hydrocarbon-hydrocarbon RDDs decrease with simulation time, indicating a reduced hydrocarbon number density around individual molecules and thus a looser molecular arrangement. This trend arises from hydrocarbon chain disentanglement induced by CO_2 dissolution, which causes oil volume swelling and viscosity reduction. Under flooding, however, the decline in peak height and area occurs more gradually than in HNP, reflecting the influence of the forward pressure gradient that suppresses oil swelling and thereby reduces hydrocarbon production (Figure S7a,b). In contrast, Figure 6b shows that the level of the CO_2-hydrocarbon RDD increases with time. During flooding, the forward pressure gradient drives more CO_2 into the pore while simultaneously hindering hydrocarbon outflow, yielding a higher RDD peak compared with that of HNP. Under HNP, by contrast, CO_2 entry depends solely on diffusion, and concurrent hydrocarbon outflow from the pore further limits CO_2 accumulation, leading to flatter, more uniform RDD profiles. Taken together, these results indicate that the forward pressure gradient during flooding enhances the accumulation of CO_2 around hydrocarbons, which increases molecular separation, reduces viscosity, and improves mobilization of heavier components. HNP, while less effective at driving CO_2 entry, facilitates hydrocarbon release due to the absence of a confining pressure gradient (Figure S7).

We also compared the interfacial and transport behaviors of CO_2 and hydrocarbons under flooding and HNP. Figure 7 shows simulation snapshots and the CO_2-oil interface evolution at T = 1 and 3 ns. In both processes, CO_2 injection initially strips adsorbed hydrocarbons into the pore center, while bulk hydrocarbons simultaneously migrate outward. Throughout, cocurrent migration of CO_2 into the dead-end nanopore occurs alongside counter-current migration of hydrocarbons out of the pore. During flooding, the forward pressure gradient drives more CO_2 into the pore, causing mutual obstruction between CO_2 and hydrocarbons and forcing hydrocarbons along tortuous migration paths. As a result, a pronounced CO_2-oil interface persists at both 1 and 3 ns. Hydrocarbon center-of-mass (COM) movement is slow (Figure S8), reflecting hindered counter-current migration and reduced hydrocarbon production. Meanwhile, cocurrent CO_2 migration dominates, leading to higher CO_2 sequestration.

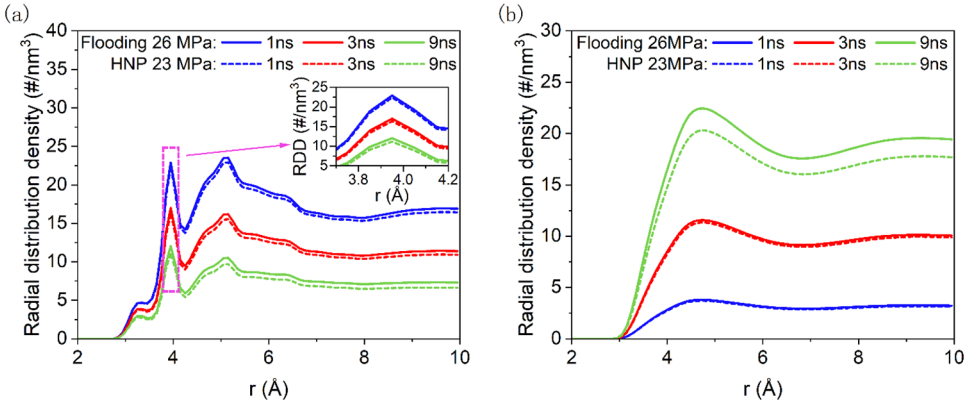


Figure 6. Radial distribution density of (a) C(hydrocarbon)-C(hydrocarbon) and (b) C(hydrocarbon)-C(CO_2).

https://doi.org/10.1021/acs.langmuir.5c05534
Langmuir 2026, 42, 4029−4042

Downloaded from pubs.acs.org/langd5/article-pdf/42/5/4029/6424108/la5c05534.pdf by PEKING UNIV user on 11 November 2026

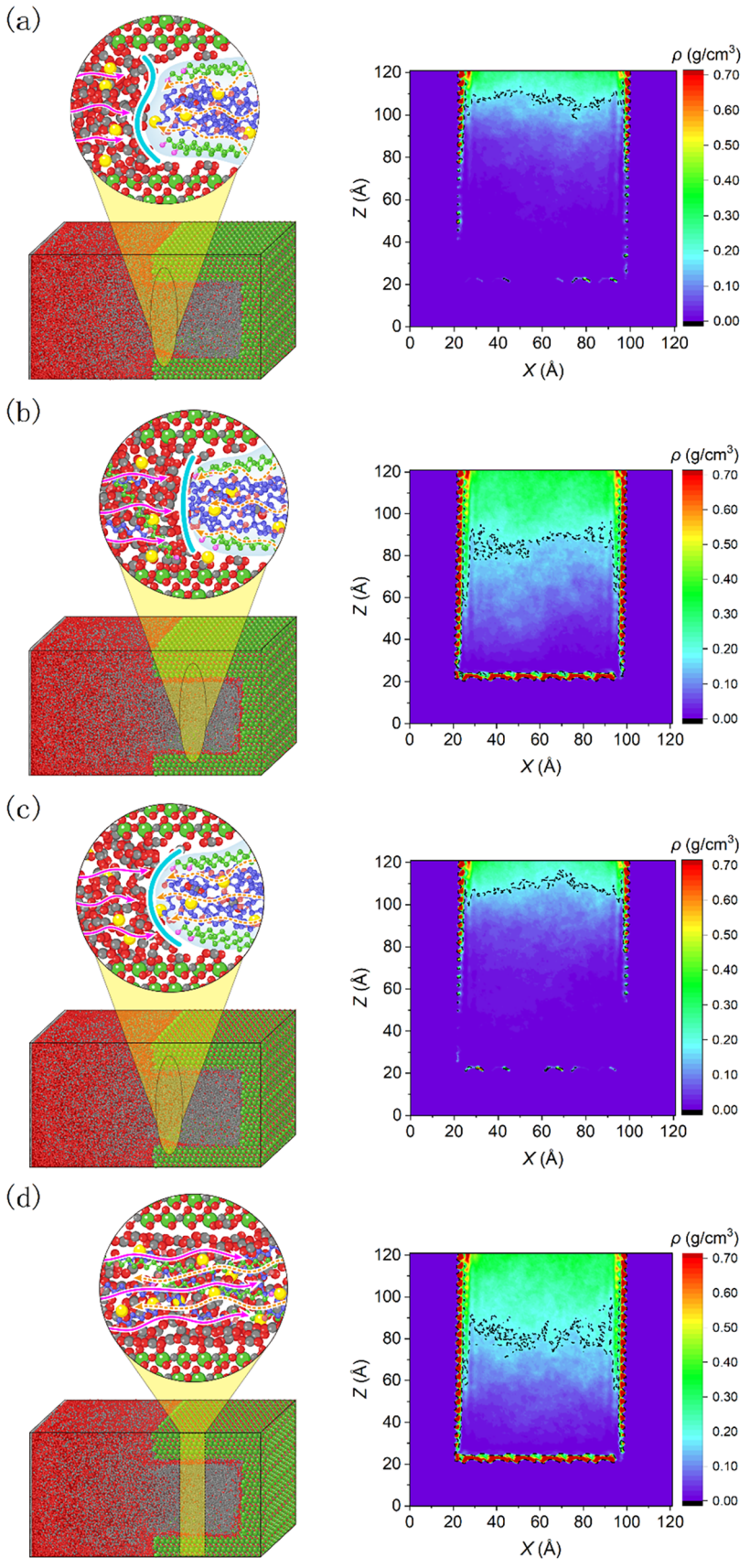


Figure 7. Simulation snapshots of oil-gas interfaces and 2-D CO_2 density contours on the $X-Z$ plane during (a, b) flooding and (c, d) HNP at 1 and 3 ns, respectively.

Downloaded from pubs.acs.org/langd5/article-pdf/42/5/4029/6424108/la5c05534.pdf by PEKING UNIV user on 11 November 2026

https://doi.org/10.1021/acs.langmuir.5c05534
Langmuir 2026, 42, 4029−4042

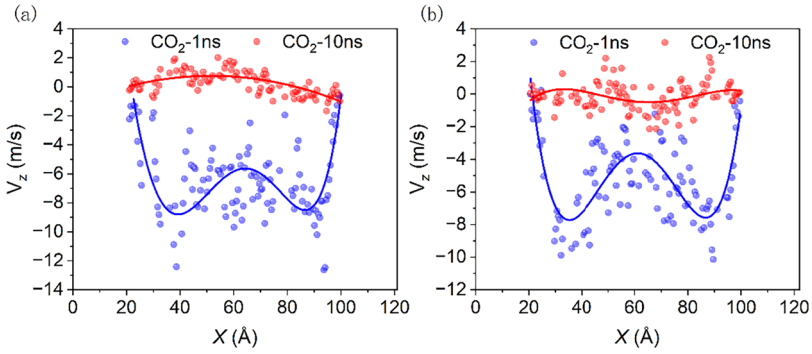


Figure 8. CO_2 migration velocity along the Z axis during (a) CO_2 flooding and (b) CO_2 HNP.

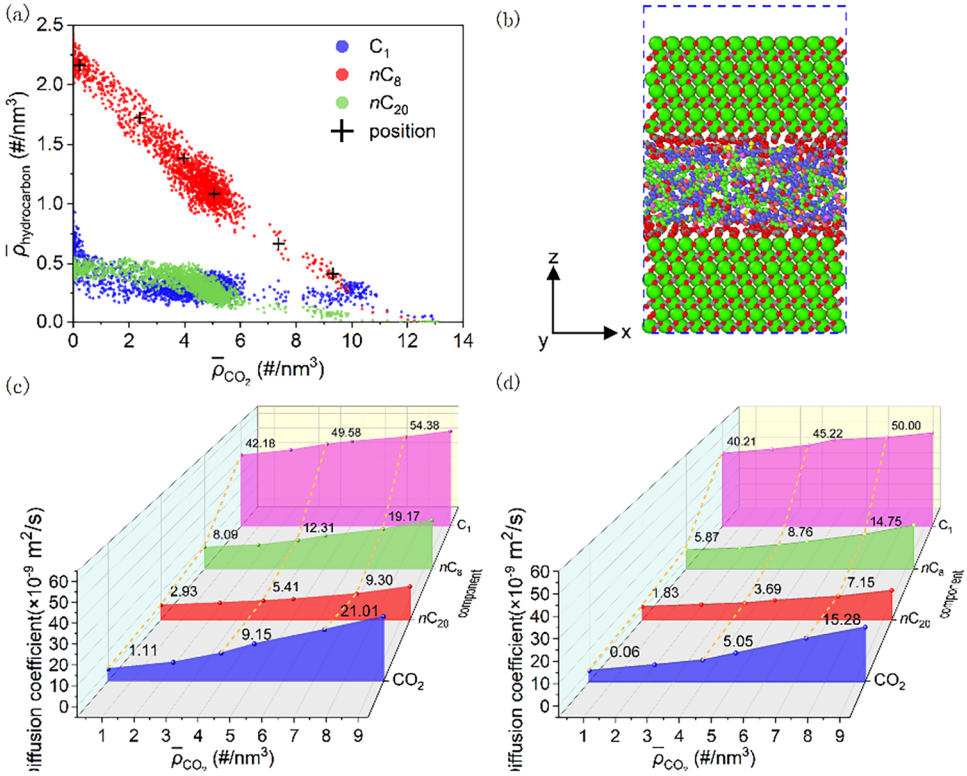


Figure 9. (a) Composition of the fluid mixture inside calcite nanopores, with each dot denoting the composition at a cross-section along the pore during the exchange process. The markers denote 6 representative locations and corresponding compositions, (b) simulation snapshots of the systems for calculate the self-diffusion coefficient of each component in calcite nanopores, (c, d) the in-plane self-diffusion coefficients of CO_2 and hydrocarbon in nanopores at 17 and 29 MPa, respectively (with components identified by markers in (a)).

In contrast, during the huff stage of the HNP, CO_2 enters the pore by spontaneous imbibition in the absence of a pressure gradient. Strong adsorption on the substrate, combined with near-miscible CO_2-oil interactions, lowers interfacial tension (IFT) and sustains cocurrent migration. Elevated reservoir temperature and pressure further enhance the CO_2-oil interactions, inducing oil volume swelling that blurs and ultimately eliminates the CO_2-oil interface by 3 ns. In the subsequent puff stage, the reverse pressure gradient accelerates hydrocarbon COM movement (Figure S8), boosting hydrocarbon production. Throughout HNP, counter-current hydrocarbon migration dominates over cocurrent CO_2 entry. Velocity profiles (Figure 8) further highlight these distinctions. At early times, CO_2 velocities near the wall and in the bulk are higher during flooding than during HNP, confirming that the forward pressure gradient promotes cocurrent CO_2 influx while suppressing hydrocarbon counter-flow. By 9 ns, flooding shows a pronounced reverse CO_2 velocity in the bulk as pressures equilibrate, whereas CO_2 and hydrocarbon velocities remain steady during HNP. This indicates that flooding delays oil swelling, requiring a longer time scale to maximize recovery from dead-end pores.

Overall, injection pressure during flooding enhances the CO_2-driven displacement of adsorbed hydrocarbons but simultaneously suppresses counter-current hydrocarbon migration. Thus, the CO_2 displacement and extraction dominate under a pressure gradient. In HNP, by contrast, oil undergoes significant swelling during the huff stage, and the reverse pressure gradient in the puff stage amplifies this effect, resulting in greater hydrocarbon mobilization and higher recovery. These findings confirm that cocurrent and counter-current flows in nanopores mutually inhibit one another,[74] with this

Downloaded from pubs.acs.org/langd5/article-pdf/42/5/4029/6424108/la5c05534.pdf by PEKING UNIV user on 11 November 2026

https://doi.org/10.1021/acs.langmuir.5c05534
Langmuir 2026, 42, 4029−4042

suppressive interaction being especially pronounced in dead-end geometries.

3.4. Diffusion Coefficient

To quantify the influence of self-diffusion on transport properties, we compute the mean squared displacement (MSD) and self-diffusion coefficient of each component (eqs 3 and 4) based on the Einstein relation.

$$\mathrm{MSD}(\triangle t) = \frac{1}{t}\int_0^t [\overrightarrow{r_{i-xy}}(t) - \overrightarrow{r_{i-xy}}(0)]^2 \mathrm{d}t = \langle[\overrightarrow{r_{i-xy}}(t) - \overrightarrow{r_{i-xy}}(0)]^2\rangle \quad (3)$$

$$D = \frac{1}{4N}\lim_{t\to\infty}\frac{\mathrm{d}}{\mathrm{d}t}\langle[\overrightarrow{r_{i-xy}}(t) - \overrightarrow{r_{i-xy}}(0)]^2\rangle \quad (4)$$

$$\overline{\rho_i}(z) = \frac{\int_0^w \rho_i(z, x)\mathrm{d}x}{w_e} \quad (5)$$

where MSD is the mean square displacement, m^2. D is the self-diffusion coefficient, m^2/s. τ and t are the total simulation time and a certain simulation moment, respectively, with the unit being s. $\overrightarrow{r_{i-xy}}(t)$ and $\overrightarrow{r_{i-xy}}(0)$ are the displacement vector of the *i-th* molecule in the $X-Y$ plane at t time and zero time, m. N is the total number of diffusion molecules in the system. $\overline{\rho_i}(z)$ is the average number density of component i within each bin along the pore depth, the bin size is 5.0 Å. $\int_0^w \rho_i(z,x)\mathrm{d}x$ is the integral of the number density distribution of component i along the X direction. w_e is the effective pore width available to the components, taken as 77.68 Å.

Following ref 75., we did not calculate self-diffusion coefficients directly from the nonequilibrium flooding and HNP, where pressure differences induce convection. Instead, we first extracted the local number density of CO_2 and each hydrocarbon and identified six recurrent composition states that represent different development stages (Figure 9a). The specific numbers are shown in Table S4 in SI. For each state, the independent equilibrium MD models with identical composition was constructed, and MSDs and self-diffusion coefficients were calculated employing (eqs 4 and 5). This two-step procedure eliminates convective contributions and yields equilibrium self-diffusion coefficients associated with the local thermodynamic states encountered during flooding and HNP. We select six recurrent positions as representative cases from which six additional independent models are constructed (Figure 9b). Figure 9c,d present the self-diffusion coefficients of each component as a function of CO_2 number density at 17 and 29 MPa, respectively. As the average CO_2 number density in the nanopore increases, adsorbed hydrocarbons desorb and migrate into the pore center, reducing mutual hindrance and enhancing diffusion coefficients for all components. Conversely, increasing the pressure from 17 to 29 MPa shortens molecular mean free paths and increases collision frequencies, lowering diffusion coefficients at comparable CO_2 densities. Across the sampled density range, the coefficients vary by roughly an order of magnitude, providing quantitative bounds for transport in the confined system. The 17 MPa curves represent upper bounds, whereas the 29 MPa curves give lower bounds for the effective self-diffusion coefficients under the pressures studied. These bounds can be directly used as input or validation data for continuum transport models.[76]

When the CO_2 density is below ~2.3 nm^{-3}, preferential adsorption on calcite leads to CO_2 diffusion coefficients lower than (or comparable to) nC_{20}. Once adsorption sites saturate and more CO_2 populates the bulk, its diffusion increases sharply. CH_4 consistently exhibits the highest diffusion coefficient, reflecting its weak affinity for calcite; increased CO_2 densities further promote CO_2−CH_4 miscibility, enhancing CH_4 diffusion. Overall, diffusion coefficients are maximized when the CO_2 concentration is highest and the hydrocarbon concentration is lowest and minimized under the opposite condition. Our results are consistent with those of Moh et al.[75] We therefore treat the results at 17 MPa (upper bound) and 29 MPa (lower bound) as effective limits for component self-diffusion in our nonequilibrium simulations, with intermediate pressures expected to yield values between these bounds. And these diffusion bounds reported here can be directly employed as pore-scale model inputs, providing physics-based parameters for cross-scale model construction and calibration.

3.5. EFFECT OF PRESSURE DIFFERENCE

Using oil recovery and CO_2 storage efficiency as performance metrics, we evaluate the effectiveness of CO_2 flooding and HNP. Oil recovery and CO_2 storage efficiency are quantified by the changes in hydrocarbon and CO_2 molecule counts within the dead-end nanopore. Parameters η and ω are defined to represent the oil recovery and CO_2 storage efficiency, respectively. The equations are as follows

$$\eta = \frac{N_{\mathrm{Bulk-Hydro}}}{N_{\mathrm{Total-Hydro}}} \quad (6)$$

$$\omega = \frac{N_{\mathrm{Pore-CO2}}}{N_{\mathrm{Total-CO2}}} \quad (7)$$

where η is oil recovery, %. $N_{\mathrm{Bulk\text{-}Hydro}}$ and $N_{\mathrm{Total\text{-}Hydro}}$ are the quantity of hydrocarbons outside the dead-end nanopore and the total number of hydrocarbons in the model, respectively. ω is the CO_2 storage efficiency, %. $N_{\mathrm{Pore\text{-}CO2}}$ and $N_{\mathrm{Total\text{-}CO2}}$ are the amount of CO_2 in the dead-end nanopore and the total number of CO_2 in the model, respectively.

At the initial state, 4800 CO_2 molecules are placed at the injection end, while the dead-end pore contains 301 CH_4, 916 nC_8, and 183 nC_{20} molecules. The pore pressure is equilibrated at 23 MPa. To establish a baseline, we first assessed hydrocarbon production under self-diffusion alone (i.e., without CO_2 injection). As shown in Figure S7, the resulting oil recovery is 8.86%, approximating natural depletion in shale reservoirs.

During the CO_2 flooding, the injection pressure is set at 26 MPa. Under these conditions, flooding recovers 194 CH_4, 523 nC_8, and 95 nC_{20} molecules (57.96% total recovery), while 2325 CO_2 molecules remain in the pore, corresponding to a storage efficiency of 48.44%. In comparison, the HNP maintains 23 MPa during the huff stage and applies a flowback pressure of 20 MPa during the puff stage. This process recovers 216 CH_4, 531 nC_8, and 75 nC_{20} molecules (58.76% recovery), with 2021 CO_2 molecules retained in the pore (45.86% storage efficiency). Thus, HNP yields a higher hydrocarbon recovery, whereas flooding favors greater CO_2 sequestration. These results align with our earlier analysis: The forward pressure gradient in flooding drives cocurrent flow, enhancing CO_2 retention, while HNP promotes counter-current migration

Downloaded from pubs.acs.org/langd5/article-pdf/42/5/4029/6424108/la5c05534.pdf by PEKING UNIV user on 11 November 2026

https://doi.org/10.1021/acs.langmuir.5c05534
Langmuir 2026, 42, 4029−4042

dominated by oil volume swelling, which improves hydrocarbon recovery from dead-end pores.

Component-specific recovery follows the order CH_4 > nC_8 > nC_{20}·CH_4, with the weakest substrate affinity and highest self-diffusion coefficient, readily migrates via diffusion and CO_2 extraction. nC_8 exhibits stronger van der Waals interactions with calcite, but CO_2 injection strips it from adsorption sites into the bulk, where chain disentanglement upon CO_2 dissolution reduces the viscosity and enhances mobility. In contrast, nC_{20} shows the lowest recovery due to its strong wall affinity and long-chain structure, which limit disentanglement and mobility; in some cases, nC_{20} aggregation may hinder flow and partially obstruct pore throats. These results confirm that CO_2 injection preferentially mobilizes light and medium hydrocarbons while leaving a substantial fraction of heavy components as residual oil. Notably, considerable medium hydrocarbons also persist after the CO_2 injection, indicating that extended flooding or multiple HNP cycles may be required for further recovery. Throughout these processes, strong CO_2-calcite interactions not only displace adsorbed hydrocarbons but also promote the attachment of CO_2 to the substrate, underpinning the dual role of CO_2 in enhancing recovery and enabling sequestration (Figure 10).

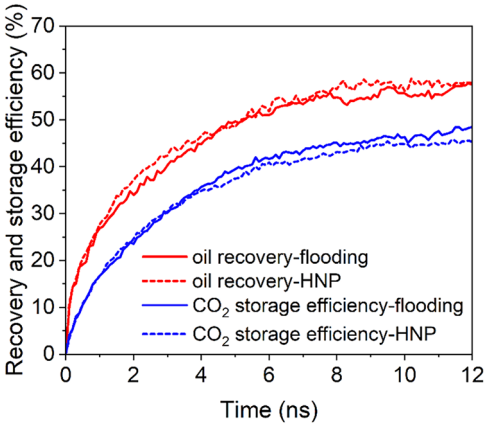


Figure 10. Shale oil recovery and CO_2 storage efficiency during CO_2 flooding and HNP.

In the middle and late stages of shale oil production, both the injection pressure during CO_2 flooding and the flowback pressure during the HNP critically influence oil recovery and CO_2 storage efficiency. To evaluate their impact, we investigated two pressure differences (3 and 6 MPa), reflecting conditions in the target reservoir. Based on these results, we further propose a hybrid development approach integrating CO_2 flooding and the HNP. Figure 11 summarizes the oil recovery and CO_2 storage efficiency for each approach and scheme. Under natural depletion (Case 0), oil recovery is minimal. In CO_2 flooding, increasing the injection pressure from 26 (Case 1) to 29 MPa (Case 2) enhances recovery to 56.58% and storage efficiency to 49.51%. In the HNP, the huff stage pressure is maintained at 23 MPa, relying solely on CO_2 diffusion into the pore. Reducing the puff-stage flowback pressure from 20 MPa (Case 3) to 17 MPa (Case 4) boosts oil recovery to 59.84% (a 50.99% increase over depletion) and storage efficiency to 44.51%. Within the tested pressure differentials, increasing the flooding pressure decreases oil recovery but enhances CO_2 storage efficiency, whereas in HNP reducing the flowback pressure has the opposite trend,

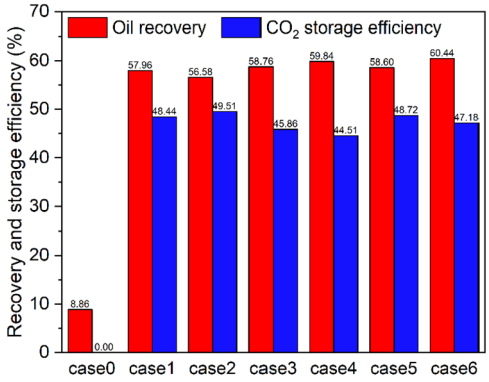


Figure 11. Oil recovery and CO_2 storage efficiency under different pressure differences and development schemes. (Case 0: depletion development. Case 1: flooding pressure = 26 MPa. Case 2: flooding pressure = 29 MPa. Case 3: HNP, injection pressure = 23 MPa (6 ns) and flowback pressure = 20 MPa (6 ns). Case 4: HNP, injection pressure = 23 MPa (6 ns) and flowback pressure = 17 MPa (6 ns). Case 5: HNP and flooding, injection pressure = 23 MPa (6 ns), flowback pressure = 20 MPa (3 ns), and flooding pressure = 26 MPa (3 ns). Case 6: flooding and HNP, flooding pressure = 26 MPa (9 ns), and flowback pressure = 20 MPa (3 ns)).

indicating that this pressure window provides a favorable operating guideline for field-scale CO_2-EOR and storage.

To further optimize the performance, two hybrid approaches were designed. In Case 5 (HNP followed by flooding), the huff stage is conducted at 23 MPa for 6 ns, followed by a puff stage at 20 MPa for 3 ns and then flooding at 26 MPa for 3 ns. In Case 6 (flooding followed by HNP), flooding at 26 MPa is applied for 3 ns, followed by a huff stage at 26 MPa for 6 ns and finally a puff stage at 20 MPa for 3 ns, effectively combining elevated huff pressure with extended soaking. As shown in Figure 11, Case 5 achieves 58.60% recovery and 48.72% storage efficiency, both higher than flooding alone. Its recovery is comparable to that of HNP alone, while its storage efficiency is improved. Case 6 achieves the best performance, with recovery reaching 60.44% (the highest among all approaches) while maintaining a high storage efficiency of 47.18%. Mechanistically, flooding creates a forward pressure gradient that drives CO_2 into the pore, mobilizing heavy hydrocarbons and improving recovery. However, excessive flooding pressure can suppress counter-current hydrocarbon migration, limiting recovery while increasing storage efficiency. In HNP, counter-current flow dominates: CO_2 dissolution induces oil swelling and mobility, while reducing puff-stage pressure further promotes hydrocarbon extraction. The hybrid approaches combine these advantages. In particular, flooding followed by a HNP (Case 6) is most effective. The initial high injection pressure enhances CO_2 dissolution, disentanglement, and viscosity reduction, while the subsequent HNP mobilizes heavy hydrocarbons and mitigates pore blockage. This synergy maximizes oil recovery while sustaining a high CO_2 storage efficiency. Taken together, this approach is readily deployable for both single-well and dual-well operations. In the single-well mode, it amounts to high injection pressure CO_2 HNP, whereas in the dual-well mode, it employs asynchronous, alternating CO_2 injection and production between adjacent wells. The hybrid approach is well-count agnostic and can be scaled to local well patterns to jointly optimize oil recovery and CO_2 storage. In addition, we quantify operational design pressure windows that are transferable to pore-scale and field-

Downloaded from pubs.acs.org/langd5/article-pdf/42/5/4029/6424108/la5c05534.pdf by PEKING UNIV user on 11 November 2026

https://doi.org/10.1021/acs.langmuir.5c05534
Langmuir 2026, 42, 4029−4042

scale studies to jointly maximize oil recovery and CO_2 storage efficiency, thereby guiding practical scheme design.

3.6. IMPLICATION

In the previous sections, we focused on the interfacial and transport behaviors of CO_2 and hydrocarbons during CO_2 flooding and HNP, elucidated the mechanisms by which CO_2 mobilizes oil in dead-end pores, and examined the effects of injection and flowback pressures on oil recovery and the CO_2 storage efficiency. Although combined approaches were tested, our performance metrics (i.e., oil recovery and CO_2 storage efficiency) consistently favored raising injection pressure and extending flooding duration before reducing flowback pressure during production.

(i) In large-scale shale oil reservoirs, early stage development benefits most from flooding between injector-producer pairs, which creates efficient flow channels and maximizes early recovery.[77] At the middle and late stages, however, residual oil remains in matrix blocks and dead-end pores outside the CO_2 sweep. At that point, injecting large pore volumes (PV) of CO_2 while shutting in producers can expand the swept volume and mobilize trapped oil.

(ii) In contrast, small-scale shale oil reservoirs may achieve rapid economic returns from HNP alone, though this primarily mobilizes oil near the wellbore.[77] Owing to the molecular dynamics time scale and computational constraints, we only simulated a single HNP cycle. However, this does not compromise interpretation of interfacial evolution or confined transport behavior, and these regularities are expected to persist across multiple cycles. Thus, increasing injection pressure, extending soaking time, and applying multiple HNP cycles can enhance oil recovery while continuously improving CO_2 storage efficiency in the long term. This approach also supports repurposing depleted reservoirs as gas storage sites (e.g., CH_4 or H_2 with CO_2 as cushion gas). In summary, injection and flowback pressures both play critical roles in shale oil development. A hybrid approach that integrates flooding and huff-and-puff effectively replenishes reservoir energy and mobilizes a larger fraction of oil, improving recovery while maintaining high CO_2 storage efficiency, particularly in the later stages of development.[77]

During CO_2 flooding and HNP, we also observed a decline in CH_4 production at late stages, suggesting that CH_4 re-enters dead-end pores and displaces nC_8. Across all development approaches, CH_4 recovery exceeds 70%, indicating substantial early mobilization. As pore and bulk pressures equilibrate later, concentration gradients drive limited CH_4 re-entry. Prior studies also show that CH_4 readily mixes with CO_2 and displaces medium hydrocarbons,[78] which may contribute to this behavior. Overall, this re-entry aids the recovery of medium hydrocarbons,[79] though its fraction remains below 10%, making it negligible in both laboratory experiments and field operations. Nevertheless, this behavior suggests that CO_2-hydrocarbon coinjection can further elevate recovery while improving energy-use efficiency and mitigating formation damage, an approach we will explore in future work.

Finally, shale oil may contain appreciable resins and asphaltenes, rendering the fluid system more complex. Based on prior work, nC_{20} can partially substitute for these heavy fractions; their presence increases wall affinity, adsorption, and transport resistance, thereby lowering EOR performance. In addition, connate water in shale oil reservoirs and residual fracturing fluids can readily trigger geochemical CO_2-water-rock reactions, significantly influencing both oil recovery and CO_2 storage efficiency during CO_2 flooding and HNP. Future work will incorporate more realistic oil components and brines, systematically quantify how oil composition and water alter oil displacement by CO_2,[73,80] and elucidate the coupled CO_2-water-rock-oil reaction-transport mechanisms that govern displacement performance.[81,82]

4. CONCLUSION

In this work, MD simulations were employed to investigate CO_2 flooding and HNP mechanisms in calcite dead-end nanopores saturated with a multicomponent shale oil. Self-diffusion coefficients of CO_2 and hydrocarbons were evaluated in equivalent equilibrium models to establish diffusion bounds, and the effects of injection and flowback pressures on oil recovery and the CO_2 storage efficiency were quantified. The main conclusions are as follows:

(i) The strongest van der Waals affinity between heavy hydrocarbons and the calcite substrate leads to the formation of solid-like nC_{20} adsorbed layers, whereas nC_8 and CH_4 predominantly reside in the pore center. CO_2 injection efficiently strips these adsorbed hydrocarbons and increases the self-diffusion coefficients of all components. Under nanoconfinement, CO_2 adsorption on the wall and CO_2 dissolution into oil are both enhanced, and the gas−liquid−solid interfacial effects become much more pronounced than in the bulk. The confinement modified the interfacial and phase behaviors jointly promote hydrocarbon mobilization and contribute to oil recovery from dead-end nanopores.

(ii) During flooding, a forward pressure gradient governs transport, driving dominant cocurrent CO_2 migration and suppressing counter-current hydrocarbon migration. This maintains a relatively clearly CO_2-oil interface and hinders the full release of oil volume swelling, which limits oil recovery but favors higher CO_2 storage efficiency. In HNP, CO_2 diffusion during the huff stage and the reverse pressure gradient during the puff stage promote counter-current hydrocarbon migration and gradual interface blurring, thereby releasing oil volume swelling more effectively. As a result, HNP achieves higher oil recovery than flooding, whereas CO_2 storage efficiency shows the opposite trend, revealing a clear trade-off between recovery and sequestration governed by nanoconfinement and interfacial effects.

(iii) The hybrid method leverages CO_2 dissolution and adsorption during the initial flooding stage together with flowback-driven oil release during the subsequent HNP stage. Flooding maximizes chain disentanglement, viscosity reduction, and oil volume swelling, while the HNP stage enhances the flow of shale oil and alleviates pore blockage. This hybrid approach increases oil recovery while maintaining substantial CO_2 storage efficiency. It is readily translatable to field operations, either as single-well HNP with elevated injection pressure or as the dual-well method with asynchronous, alternating CO_2 injection and production, providing a practical basis for full-chain CCUS process design.

Downloaded from pubs.acs.org/langd5/article-pdf/42/5/4029/6424108/la5c05534.pdf by PEKING UNIV user on 11 November 2026

https://doi.org/10.1021/acs.langmuir.5c05534
Langmuir 2026, 42, 4029−4042

While our study provides molecular-scale insights into the CO_2-EOR in calcite dead-end nanopores, it is limited to saturated hydrocarbons and a calcite substrate. Real reservoirs contain aromatics, resins, asphaltenes, formation water, and diverse minerals and ions, all of which affect wettability, phase behavior, and miscibility. Future work will incorporate more realistic oil compositions, brine, and mineralogical heterogeneity, as well as more complex pore structures, to better represent reservoir conditions and support upscaling from MD to pore-scale and core-scale simulations and field operations. In particular, the bulk CO_2-oil phase and miscibility behavior will be explicitly compared with nanoconfined behavior, and MD informed transport models will be coupled with pore-scale and core-scale experiments to benchmark and refine the simulation methods and results responses. These molecular-scale insights form a foundation for designing more effective CO_2-EOR strategies and optimizing GCS in shale reservoirs, thereby enabling process integration and overall climate mitigation performance.

■ ASSOCIATED CONTENT

Supporting Information

The Supporting Information is available free of charge at https://pubs.acs.org/doi/10.1021/acs.langmuir.5c05534.

Force field parameters; model validation (CO_2 and hydrocarbon density validation, force field validation, piston method validation); evidence for reaching equilibrium; 2D density contours of CO_2 flooding and HNP; variations in CO_2 and hydrocarbon molecule numbers at different pressures; center of mass changes of CO_2 and hydrocarbon molecules during flooding and HNP; CO_2 and hydrocarbon molecule counts in the diffusion models; molecular diffusion of pure hydrocarbon into vacuum (PDF)

■ AUTHOR INFORMATION

Corresponding Authors

Keliu Wu − *State Key Laboratory of Petroleum Resources and Engineering, China University of Petroleum (Beijing), Beijing 102249, China;* orcid.org/0000-0002-0021-5007; Email: kwu@cup.edu.cn

Zhehui Jin − *Department of Civil and Environmental Engineering, School of Mining and Petroleum Engineering, University of Alberta, Edmonton, Alberta T6G 1H9, Canada;* orcid.org/0000-0001-8305-5637; Email: zhehui2@ualberta.ca

Authors

Shiqiang Guo − *State Key Laboratory of Petroleum Resources and Engineering, China University of Petroleum (Beijing), Beijing 102249, China; Department of Civil and Environmental Engineering, School of Mining and Petroleum Engineering, University of Alberta, Edmonton, Alberta T6G 1H9, Canada;* orcid.org/0009-0008-1626-2546

Qingyuan Zhu − *State Key Laboratory of Petroleum Resources and Engineering, China University of Petroleum (Beijing), Beijing 102249, China; Department of Civil and Environmental Engineering, School of Mining and Petroleum Engineering, University of Alberta, Edmonton, Alberta T6G 1H9, Canada;* orcid.org/0000-0001-6127-4660

Dong Feng − *School of Energy Resources, China University of Geosciences (Beijing), Beijing 100083, China*

Juan Luo − *Research Institute of Petroleum Engineering Technology, Shengli Oilfield Branch, China Petroleum & Chemical Corporation, Dongying, Shandong 257000, China*

Shengting Zhang − *State Key Laboratory of Petroleum Resources and Engineering, China University of Petroleum (Beijing), Beijing 102249, China*

Linghao Peng − *State Key Laboratory of Petroleum Resources and Engineering, China University of Petroleum (Beijing), Beijing 102249, China*

Yaowei Huang − *State Key Laboratory of Petroleum Resources and Engineering, China University of Petroleum (Beijing), Beijing 102249, China*

Ke Xu − *Department of Energy and Resources Engineering, College of Engineering, Peking University, Beijing 100871, China*

Complete contact information is available at: https://pubs.acs.org/10.1021/acs.langmuir.5c05534

Notes

The authors declare no competing financial interest.

■ ACKNOWLEDGMENTS

S.G. was supported by the China Scholarship Council (Student Number: 202406440020). The authors also acknowledge the support of the National Natural Science Foundation of China (Nos. 52174041, 52204058), the Fundamental Research Funds for the Central Universities (No. 2652023047), and a Discovery Grant from the Natural Sciences and Engineering Research Council of Canada (NSERC RGPIN-2023-03587).

■ REFERENCES

(1) Zheng, X.; Streimikiene, D.; Balezentis, T.; Mardani, A.; Cavallaro, F.; Liao, H. A Review of Greenhouse Gas Emission Profiles, Dynamics, and Climate Change Mitigation Efforts across the Key Climate Change Players. *J. Cleaner Prod.* **2019**, *234*, 1113−1133.

(2) Ofiti, N. O. E.; Schmidt, M. W. I.; Abiven, S.; Hanson, P. J.; Iversen, C. M.; Wilson, R. M.; Kostka, J. E.; Wiesenberg, G. L. B.; Malhotra, A. Climate Warming and Elevated CO2 Alter Peatland Soil Carbon Sources and Stability. *Nat. Commun.* **2023**, *14* (1), No. 7533.

(3) Filonchyk, M.; Peterson, M. P.; Zhang, L.; Hurynovich, V.; He, Y. Greenhouse Gases Emissions and Global Climate Change: Examining the Influence of CO2, CH4, and N2O. *Sci. Total Environ.* **2024**, *935*, No. 173359.

(4) Althor, G.; Watson, J. E. M.; Fuller, R. A. Global Mismatch between Greenhouse Gas Emissions and the Burden of Climate Change. *Sci. Rep.* **2016**, *6* (1), No. 20281.

(5) Hu, Y.; Hao, M.; Chen, G.; Sun, R.; Li, S. Technologies and practice of CO2 flooding and sequestration in China. *Pet. Explor. Dev.* **2019**, *46* (4), 753−766.

(6) Shi, Q.; Zheng, B.; Zheng, Y.; Tong, D.; Liu, Y.; Ma, H.; Hong, C.; Geng, G.; Guan, D.; He, K.; Zhang, Q. Co-Benefits of CO2 Emission Reduction from China's Clean Air Actions between 2013−2020. *Nat. Commun.* **2022**, *13* (1), No. 5061.

(7) Jia, C. Prospects and Five Future Theoretical and Technical Challenges of the Upstream Petroleum Industry in China. *Acta Pet. Sin.* **2024**, *45* (1), 1−14.

(8) Shen, P.; Liao, X. *The Technology of Carbon Dioxide Stored in Geological Media and Enhanced Oil Recovery*; Petroleum Industry Press: Beijing, 2009.

(9) Hu, Y.; Hao, M.; Chen, G. *Technology of Enhanced Oil Recovery by Carbon Dioxide*; Beijing: Petroleum Industry Press: Beijing, 2018.

(10) Song, X.; Wang, F.; Ma, D.; Gao, M.; Zhang, Y. Progress and prospect of carbon dioxide capture, utilization and storage in CNPC oilfields. *Pet. Explor. Dev.* **2023**, *50* (1), 229−244.

Downloaded from pubs.acs.org/langd5/article-pdf/42/5/4029/6424108/la5c05534.pdf by PEKING UNIV user on 11 November 2026

(11) International Energy Agency (IEA). *CCUS in Clean Energy Transitions*; Special Report on Carbon Capture Utilisation and Storage Energy Technology Perspectives 2020; IEA: Paris, 2020 https://www.IEA.org/reports/ccus-in-clean-energy-transitions.
(12) Zou, C.; Pan, S.; Jing, Z.; Gao, J.; Yang, Z.; Wu, S.; Zhao, Q. Shale Oil and Gas Revolution and Its Impact. *Acta Pet. Sin.* **2020**, *41* (1), 1−12.
(13) Feng, Q.; Xu, S.; Xing, X.; Zhang, W.; Wang, S. Advances and Challenges in Shale Oil Development: A Critical Review. *Adv. Geo-Energy Res.* **2020**, *4* (4), 406−418.
(14) Xia, X.; Jiao, X.; Li, J.; Shen, W.; Xia, Y.; Wang, H. Gas Adsorption Behavior in Shale Reservoirs: Insights from Molecular Scale. *Capillarity* **2024**, *13* (3), 68−72.
(15) Zhang, S.; Yan, J.; Hu, Q.; Wang, J.; Tian, T.; Chao, J.; Wang, M. Integrated NMR and FE-SEM Methods for Pore Structure Characterization of Shahejie Shale from the Dongying Depression, Bohai Bay Basin. *Mar. Pet. Geol.* **2019**, *100*, 85−94.
(16) Liu, B.; Sun, J.; Zhang, Y.; He, J.; Fu, X.; Yang, L.; Xing, J.; Zhao, X. Reservoir Space and Enrichment Model of Shale Oil in the First Member of Cretaceous Qingshankou Formation in the Changling Sag, Southern Songliao Basin, NE China. *Pet. Explor. Dev.* **2021**, *48* (3), 608−624.
(17) Zhang, L.; Yu, X.; Dong, H.; Li, Y. Molecular Dynamics of Mass Transfer between CO2 and Shale Oil under Confinement Effect. *J. China Univ. Pet. Ed. Nat. Sci.* **2024**, 1−9.
(18) Jia, B.; Yang, Y.; Li, C.; Wei, J.; Rabatuly, M.; Wang, L. A Comprehensive Review of Shale Wettability Characterization: Mechanisms, Measurements and Influencing Factors. *Capillarity* **2025**, *17* (2), 38−53.
(19) Zhu, C.; Guo, W.; Li, Y.; Gong, H.; Sheng, J. J.; Dong, M. Effect of Occurrence States of Fluid and Pore Structures on Shale Oil Movability. *Fuel* **2021**, *288*, No. 119847.
(20) Shao, X.; Wang, K.; Zhao, L.; Su, C.; Zhang, D.; Gao, W. Effects of Salinity and Driving Pressure on Water Imbibition during Shale Formation. *Capillarity* **2024**, *11* (3), 70−80.
(21) Wang, R.; Bi, S.; Guo, Z.; Feng, G. Molecular Insight into Replacement Dynamics of CO2 Enhanced Oil Recovery in Nanopores. *Chem. Eng. J.* **2022**, *440*, No. 135796.
(22) Song, Y.; Song, Z.; Chen, Z.; Zhang, L.; Zhang, Y.; Feng, D.; Wu, Z.; Wu, J. Fluid Phase Behavior in Multi-Scale Shale Reservoirs with Nano-Confinement Effect. *Energy* **2024**, *289*, No. 130027.
(23) Lashgari, H. R.; Sun, A.; Zhang, T.; Pope, G. A.; Lake, L. W. Evaluation of Carbon Dioxide Storage and Miscible Gas EOR in Shale Oil Reservoirs. *Fuel* **2019**, *241*, 1223−1235.
(24) Jia, B.; Tsau, J.-S.; Barati, R. A Review of the Current Progress of CO2 Injection EOR and Carbon Storage in Shale Oil Reservoirs. *Fuel* **2019**, *236*, 404−427.
(25) Wu, Z.; Sun, Z.; Shu, K.; Jiang, S.; Gou, Q.; Chen, Z. Mechanism of Shale Oil Displacement by CO2 in Nanopores: A Molecular Dynamics Simulation Study. *Adv. Geo-Energy Res.* **2024**, *11* (2), 141−151.
(26) Moh, D. Y.; Zhang, H.; Wang, S.; Yin, X.; Qiao, R. Soaking in CO2 Huff-n-Puff: A Single-Nanopore Scale Study. *Fuel* **2022**, *308*, No. 122026.
(27) Zhang, H.; Gong, H.; Lv, W.; Lv, J.; Gao, M.; Wu, S.; Sun, H.; Xu, L.; Dong, M. Influence of Glycol Ether Additive with Low Molecular Weight on the Interactions between CO2 and Oil: Applications for Enhanced Shale Oil Recovery. *Pet. Sci.* **2024**, *21* (5), 3401−3416.
(28) Liu, B.; Shi, J.; Sun, B.; Shen, Y.; Zhang, J.; Chen, X.; Wang, M. Molecular Dynamics Simulation on Volume Swelling of CO2−Alkane System. *Fuel* **2015**, *143*, 194−201.
(29) Dong, X.; Xu, W.; Liu, H.; Chen, Z.; Lu, N.; Wang, W. On the Replacement Behavior of CO2 in Nanopores of Shale Oil Reservoirs: Insights from Wettability Tests and Molecular Dynamics Simulations. *Geoenergy Sci. Eng.* **2023**, *223*, No. 211528.
(30) Li, C.; Pu, H.; Zhong, X.; Li, Y.; Zhao, J. X. Interfacial Interactions between Bakken Crude Oil and Injected Gases at Reservoir Temperature: A Molecular Dynamics Simulation Study. *Fuel* **2020**, *276*, No. 118058.
(31) Tang, R.; Hou, D.; Wang, Y.; Zhu, H.; Gong, F. Molecular Simulation of CO2−Hydrocarbon Minimum Miscibility Pressure in Tight Reservoir Nanopores under Varying Wettability Conditions. *Chem. Eng. Sci.* **2026**, *321*, No. 122730.
(32) Kim, T. H.; Cho, J.; Lee, K. S. In *Modeling of CO2 Flooding and Huff and Puff Considering Molecular Diffusion and Stress-Dependent Deformation in Tight Oil Reservoir*; SPE Europec featured at 79th EAGE Conference and Exhibition OnePetro: Paris, France, 2017.; p D022S013R003.
(33) Afari, S.; Ling, K.; Sennaoui, B.; Maxey, D.; Oguntade, T.; Porlles, J. Optimization of CO2 Huff-n-Puff EOR in the Bakken Formation Using Numerical Simulation and Response Surface Methodology. *J. Pet. Sci. Eng.* **2022**, *215*, No. 110552.
(34) Song, Y.; Yao, C.; Zhang, X.; Zhao, J.; Chen, N.; Hou, J.; Yang, H. Three-Dimensional Physical Experimental Study on Mechanisms and Influencing Factors of CO2 Huff-n-Puff and Flooding Process in Shale Reservoirs after Fracturing. *Geoenergy Sci. Eng.* **2024**, *243*, No. 213376.
(35) Wan, Y.; Jia, C.; Lv, W.; Jia, N.; Jiang, L.; Wang, Y. Recovery Mechanisms and Formation Influencing Factors of Miscible CO2 Huff-n-Puff Processes in Shale Oil Reservoirs: A Systematic Review. *Adv. Geo-Energy Res.* **2024**, *11* (2), 88−102.
(36) Tang, W.; Sheng, J. J. Huff-n-Puff Gas Injection or Gas Flooding in Tight Oil Reservoirs? *J. Pet. Sci. Eng.* **2022**, *208*, No. 109725.
(37) Li, L.; Su, Y.; Sheng, J. J.; Hao, Y.; Wang, W.; Lv, Y.; Zhao, Q.; Wang, H. Experimental and Numerical Study on CO_2 Sweep Volume during CO_2 Huff-n-Puff Enhanced Oil Recovery Process in Shale Oil Reservoirs. *Energy Fuels* **2019**, *33* (5), 4017−4032.
(38) Liu, J.; Li, H.; Tan, Q.; Liu, S.; Zhao, H.; Wang, Z. Quantitative Study of CO2 Huff-n-Puff Enhanced Oil Recovery in Tight Formation Using Online NMR Technology. *J. Pet. Sci. Eng.* **2022**, *216*, No. 110688.
(39) Peng, X.; Wang, Y.; Diao, Y.; Zhang, L.; Yazid, I. M.; Ren, S. Experimental Investigation on the Operation Parameters of Carbon Dioxide Huff-n-Puff Process in Ultra Low Permeability Oil Reservoirs. *J. Pet. Sci. Eng.* **2019**, *174*, 903−912.
(40) Nguyen, P.; Carey, J. W.; Viswanathan, H. S.; Porter, M. Effectiveness of Supercritical-CO2 and N2 Huff-and-Puff Methods of Enhanced Oil Recovery in Shale Fracture Networks Using Microfluidic Experiments. *Appl. Energy* **2018**, *230*, 160−174.
(41) Yu, W.; Lashgari, H. R.; Wu, K.; Sepehrnoori, K. CO2 Injection for Enhanced Oil Recovery in Bakken Tight Oil Reservoirs. *Fuel* **2015**, *159*, 354−363.
(42) Zuloaga, P.; Yu, W.; Miao, J.; Sepehrnoori, K. Performance Evaluation of CO2 Huff-n-Puff and Continuous CO2 Injection in Tight Oil Reservoirs. *Energy* **2017**, *134*, 181−192.
(43) Song, Y.; Song, Z.; Chen, Z.; Mo, Y.; Zhou, Q.; Tian, S. Simulation of CO2 Enhanced Oil Recovery and Storage in Shale Oil Reservoirs: Unveiling the Impacts of Nano-Confinement and Oil Composition. *Adv. Geo-Energy Res.* **2024**, *13* (2), 106−118.
(44) Wang, H.; Su, Y.; Wang, W.; Jin, Z.; Chen, H. CO2-Oil Diffusion, Adsorption and Miscible Flow in Nanoporous Media from Pore-Scale Perspectives. *Chem. Eng. J.* **2022**, *450*, No. 137957.
(45) Wang, L.; Zhang, Y.-F.; Zou, R.; Yuan, Y.-F.; Zou, R.; Huang, L.; Liu, Y.-S.; Ding, J.-C.; Meng, Z. Applications of Molecular Dynamics Simulation in Studying Shale Oil Reservoirs at the Nanoscale: Advances, Challenges and Perspectives. *Pet. Sci.* **2025**, *22* (1), 234−254.
(46) Huang, L.; Ning, Z.; Wang, Q.; Zhang, W.; Cheng, Z.; Wu, X.; Qin, H. Effect of Organic Type and Moisture on CO2/CH4 Competitive Adsorption in Kerogen with Implications for CO2 Sequestration and Enhanced CH4 Recovery. *Appl. Energy* **2018**, *210*, 28−43.
(47) Zhang, M.; Zhan, S.; Jin, Z. Recovery Mechanisms of Hydrocarbon Mixtures in Organic and Inorganic Nanopores during

Downloaded from pubs.acs.org/langd5/article-pdf/42/5/4029/6421089/la5c05534.pdf by PEKING UNIV user on 11 November 2026

https://doi.org/10.1021/acs.langmuir.5c05534
Langmuir 2026, 42, 4029−4042

Pressure Drawdown and CO2 Injection from Molecular Perspectives. *Chem. Eng. J.* **2020**, *382*, No. 122808.
(48) Zhang, W.; Feng, Q.; Wang, S.; Xing, X.; Jin, Z. CO2-Regulated Octane Flow in Calcite Nanopores from Molecular Perspectives. *Fuel* **2021**, *286*, No. 119299.
(49) Liu, B.; Wang, C.; Zhang, J.; Xiao, S.; Zhang, Z.; Shen, Y.; Sun, B.; He, J. Displacement Mechanism of Oil in Shale Inorganic Nanopores by Supercritical Carbon Dioxide from Molecular Dynamics Simulations. *Energy Fuels* **2017**, *31* (1), 738−746.
(50) Wang, T.; Tian, K.; Li, N.; Ma, Z.; Zhang, J.; Tian, S. *CO2 Utilization and Sequestration in Kerogen Nanopores: A Nanoscale Study in Shale Reservoirs.*; Elsevier, 2025; p 21.
(51) Moh, D. Y.; Fang, C.; Yin, X.; Qiao, R. Interfacial CO_2–Mediated Nanoscale Oil Transport: From Impediment to Enhancement. *Phys. Chem. Chem. Phys.* **2020**, *22* (40), 23057−23063.
(52) Huang, T.; Cheng, L.; Cao, R.; Wang, X.; Jia, P.; Cao, C. Molecular Simulation of the Dynamic Distribution of Complex Oil Components in Shale Nanopores during CO2-EOR. *Chem. Eng. J.* **2024**, *479*, No. 147743.
(53) Liang, Y.; Wang, S.; Feng, Q.; Zhang, M.; Cao, X.; Wang, X. Ultrahigh-Resolution Reconstruction of Shale Digital Rocks from FIB-SEM Images Using Deep Learning. *SPE J.* **2024**, *29* (03), 1434−1450.
(54) Chen, F.; Wang, S.; Nasrabadi, H. Molecular Insights of Excessive Water Cut during Cyclic Gas Injection in Liquid-Rich Shale Reservoirs: Contributions of Hydrocarbon Condensation and Water Trapping. *SPE J.* **2024**, *29* (06), 3223−3237.
(55) Wang, S.; Zhang, M.; Zhang, Y.; Lei, Z.; Feng, Q.; Xu, S.; Zhang, J. Mechanisms of CO2 Huff and Puff Enhanced Oil Recovery and Storage within Shale Nanopores. *Chem. Eng. J.* **2025**, *506*, No. 160098.
(56) Guo, S.; Wu, K.; Zhu, Q.; Zhang, S.; Ran, H.; Li, K.; Jiang, J.Study on the Miscible Behavior of CO2 Flooding with Different Water Saturation in Low-Permeability Reservoirs *Energy Proceedings* 2025, p 50.
(57) Ohnesorge, F.; Binnig, G. True Atomic Resolution by Atomic Force Microscopy Through Repulsive and Attractive Forces. *Science* **1993**, *260* (5113), 1451−1456.
(58) Blanchard, D. L.; Baer, D. R. The Interactions of Co, Mn and Water with Calcite Surfaces. *Surf. Sci.* **1992**, *276* (1−3), 27−39.
(59) Xiao, S.; Edwards, S. A.; Gräter, F. A New Transferable Forcefield for Simulating the Mechanics of $CaCO_3$ Crystals. *J. Phys. Chem. C* **2011**, *115* (41), 20067−20075.
(60) Santos, M. S.; Franco, L. F. M.; Castier, M.; Economou, I. G. Molecular Dynamics Simulation of *n* -Alkanes and CO_2 Confined by Calcite Nanopores. *Energy Fuels* **2018**, *32* (2), 1934−1941.
(61) Jorgensen, W. L.; Madura, J. D.; Swenson, C. J. Optimized Intermolecular Potential Functions for Liquid Hydrocarbons. *J. Am. Chem. Soc.* **1984**, *106* (22), 6638−6646.
(62) Potoff, J. J.; Siepmann, J. I. Vapor−Liquid Equilibria of Mixtures Containing Alkanes, Carbon Dioxide, and Nitrogen. *AIChE J.* **2001**, *47* (7), 1676−1682.
(63) Hoover, W. G. Canonical Dynamics: Equilibrium Phase-Space Distributions. *Phys. Rev. A* **1985**, *31* (3), No. 1695.
(64) Lorenz, C. D.; Crozier, P. S.; Anderson, J. A.; Travesset, A. Molecular Dynamics of Ionic Transport and Electrokinetic Effects in Realistic Silica Channels. *J. Phys. Chem. C* **2008**, *112* (27), 10222−10232.
(65) Haria, N. R.; Lorenz, C. D. Atomistic Description of Pressure-Driven Flow of Aqueous Salt Solutions through Charged Silica Nanopores. *J. Phys. Chem. C* **2015**, *119* (22), 12298−12311.
(66) Li, Z.; Jun Yao; Kou, J. Mixture Composition Effect on Hydrocarbon−Water Transport in Shale Organic Nanochannels. *J. Phys. Chem. Lett.* **2019**, *10* (15), 4291−4296.
(67) Plimpton, S. Fast Parallel Algorithms for Short-Range Molecular Dynamics. *J. Comput. Phys.* **1995**, *117* (1), 1−19.
(68) Jewett, A. I.; Stelter, D.; Lambert, J.; Saladi, S. M.; Roscioni, O. M.; Ricci, M.; Autin, L.; Maritan, M.; Bashusqeh, S. M.; Keyes, T.; Dame, R. T.; Shea, J.-E.; Jensen, G. J.; Goodsell, D. S. Moltemplate: A Tool for Coarse-Grained Modeling of Complex Biological Matter and Soft Condensed Matter Physics. *J. Mol. Biol.* **2021**, *433* (11), No. 166841.
(69) Stukowski, A. Visualization and Analysis of Atomistic Simulation Data with OVITO−the Open Visualization Tool. *Model. Simul. Mater. Sci. Eng.* **2010**, *18* (1), No. 015012.
(70) Eastwood, J. W.; Hockney, R. W.; Lawrence, D. N. P3M3DP-The three-dimensional periodic particle-particle/particle-mesh program. *Comput. Phys. Commun.* **1980**, *19* (2), 215−261.
(71) Oh, S. H.; Chisholm, M. F.; Kauffmann, Y.; Kaplan, W. D.; Luo, W.; Rühle, M.; Scheu, C. Oscillatory Mass Transport in Vapor-Liquid-Solid Growth of Sapphire Nanowires. *Science* **2010**, *330* (6003), 489−493.
(72) Jin, Z.; Firoozabadi, A. Phase Behavior and Flow in Shale Nanopores from Molecular Simulations. *Fluid Phase Equilib.* **2016**, *430*, 156−168.
(73) Luo, Y.; Liu, X.; Xiao, H.; Zheng, T. Microscopic Production Characteristics of Tight Oil in the Nanopores of Different CO2-Affected Areas from Molecular Dynamics Simulations. *Sep. Purif. Technol.* **2023**, *306*, No. 122607.
(74) Jiang, W.; Lv, W.; Jia, N.; Cheng, K.; Wan, Y.; Wang, K. Molecular Insights into Soaking in Hybrid N_2 − CO_2 Huff-n-Puff: A Case Study of a Single Quartz Nanopore-Hydrocarbon System. *Langmuir* **2024**, *40* (29), 14922−14940.
(75) Moh, D. Y.; Zhang, H.; Sun, S.; Qiao, R. Molecular Anatomy and Macroscopic Behavior of Oil Extraction from Nanopores by CO2 and CH4. *Fuel* **2022**, *324*, No. 124662.
(76) Babatunde, K. A.; Emami-Meybodi, H. Transport of Binary Gases in Nanoporous Media with Non-Equilibrium Adsorption. *Appl. Surf. Sci. Adv.* **2025**, *28*, No. 100808.
(77) Li, Y.; Huang, W.; Jin, Y.; He, Y.; Chen, Z.; Tang, Y.; Wu, G. Different Reservoir Types of CO2 Flooding in Sinopec EOR Technology Development and Application under "Dual Carbon" Vision. *Pet. Reserv. Eval. Dev.* **2021**, *11* (6), 793−804.
(78) Wang, P.; Li, X.; Tao, Z.; Wang, S.; Fan, J.; Feng, Q.; Xue, Q. The Miscible Behaviors and Mechanism of CO2/CH4/C3H8/N2 and Crude Oil in Nanoslits: A Molecular Dynamics Simulation Study. *Fuel* **2021**, *304*, No. 121461.
(79) Yan, Y.; Jia, Z.; Geng, X.; Liang, D.; Hao, X.; Yang, Z.; Ding, B. Insight into Miscibility Mechanism of Multiple Components Crude Oil in CO2/CH4 by Molecular Dynamic Simulation. *J. Mol. Liq.* **2024**, *398*, No. 124283.
(80) Luan, Y.; Dou, X.; Zhou, Y.; Hao, P.; Liu, B.; Liu, J. Effect of the Water Film Rupture on the Oil Displacement by Supercritical CO_2 in the Nanopore: Molecular Dynamics Simulations. *Energy Fuels* **2022**, *36* (8), 4348−4357.
(81) Yu, Z.; Liu, L.; Liu, K.; Yang, S.; Yang, Y. Petrological Characterization and Reactive Transport Simulation of a High-Water-Cut Oil Reservoir in the Southern Songliao Basin, Eastern China for CO2 Sequestration. *Int. J. Greenhouse Gas Control* **2015**, *37*, 191−212.
(82) Cui, G.; Yang, L.; Fang, J.; Qiu, Z.; Wang, Y.; Ren, S. Geochemical Reactions and Their Influence on Petrophysical Properties of Ultra-Low Permeability Oil Reservoirs during Water and CO2 Flooding. *J. Pet. Sci. Eng.* **2021**, *203*, No. 108672.

Downloaded from pubs.acs.org/langd5/article-pdf/42/5/4029/6424108/la5c05534.pdf by PEKING UNIV user on 11 November 2026

https://doi.org/10.1021/acs.langmuir.5c05534
Langmuir 2026, 42, 4029−4042